

## Internal Balance during Low-Voltage-Ride-Through of the Modular Multilevel Converter STATCOM

Tsolaridis, Georgios; Kontos, Epameinondas; Chaudhary, Sanjay K.; Bauer, Pavol; Teodorescu, Remus

**DOI**

[10.3390/en10070935](https://doi.org/10.3390/en10070935)

**Publication date**

2017

**Document Version**

Final published version

**Published in**

Energies

**Citation (APA)**

Tsolaridis, G., Kontos, E., Chaudhary, S. K., Bauer, P., & Teodorescu, R. (2017). Internal Balance during Low-Voltage-Ride-Through of the Modular Multilevel Converter STATCOM. *Energies*, 10(7), 1-18. Article 935. <https://doi.org/10.3390/en10070935>

**Important note**

To cite this publication, please use the final published version (if applicable).  
Please check the document version above.

**Copyright**

Other than for strictly personal use, it is not permitted to download, forward or distribute the text or part of it, without the consent of the author(s) and/or copyright holder(s), unless the work is under an open content license such as Creative Commons.

**Takedown policy**

Please contact us and provide details if you believe this document breaches copyrights.  
We will remove access to the work immediately and investigate your claim.

## Article

# Internal Balance during Low-Voltage-Ride-Through of the Modular Multilevel Converter STATCOM

Georgios Tsolaridis <sup>1</sup>, Epameinondas Kontos <sup>2,\*</sup>, Sanjay K. Chaudhary <sup>1</sup>, Pavol Bauer <sup>2</sup> and Remus Teodorescu <sup>1</sup>

<sup>1</sup> Department of Energy Technology, Aalborg University, 9220 Aalborg East, Denmark; g.tsolaridis@gmail.com (G.T.); Skc@et.aau.dk (S.K.C.); ret@et.aau.dk (R.T.)

<sup>2</sup> Department of Electrical Sustainable Energy, Delft University of Technology, 2628 CD Delft, The Netherlands; p.bauer@tudelft.nl

\* Correspondence: e.kontos@tudelft.nl; Tel.: +31-(0)15-2785744; Fax: +31-(0)15-2781182

Received: 9 May 2017 ; Accepted: 3 July 2017; Published: 5 July 2017

**Abstract:** Grid faults are common in power systems and can have a severe impact on the operation of the converters in the system. In this paper, the operation of a Modular Multilevel Converter (MMC)-based Static Synchronous Compensators (STATCOM) is investigated during grid faults. The study focuses on the challenging internal control of the converter to allow the independent control of the energy levels of each arm, with the goal to maintain internal balancing of the MMC during contingencies. Extensive experimental results highlight the need for a sophisticated internal control. Moreover, the experimental analysis verifies that, by using the proposed control structure, the MMC can effectively ride through a fault on the AC side without tripping, while injecting the necessary positive and negative sequence reactive current levels according to the most recent grid codes.

**Keywords:** arm energy balance; circulating current controller; grid asymmetries; low-voltage ride-through; modular multilevel converter; STATCOM

## 1. Introduction

Static Synchronous Compensators (STATCOMs) are used in applications where fast dynamic reactive current injection is needed. Mitigation of fast voltage variations due to grid faults or compensation of disturbances produced by rapidly varying loads, like arc furnaces, are conventional applications where STATCOMs are used [1].

Recently, the Multilevel Modular Converter (MMC) technology [2–4] has successfully replaced the conventional two-level topology in Medium- and High-Voltage DC (MVDC and HVDC) applications due to its superior performance in terms of efficiency, injected voltage harmonics, environmental footprint, modularity and fault tolerance. The topology with Full-Bridge (FB) submodules in Delta connection (FB-D) [5–8] is well suited for STATCOM applications, as it allows the handling of positive and negative sequence current at the same time with a smaller initial cost [9]. Additionally, other proposals such as the FB submodules in Double-Star connection (FB-DS) have been reported [10–12]. However, the high number of power devices reduces the topology practicability.

Another attractive STATCOM configuration is the Double-Star (DS) topology of the MMC using Half-Bridge (HB) submodules [13,14]. The DS-MMC was proven to be superior against the FB-D when the focus is laid on negative sequence current injection [15]. Nevertheless, high power quality is a major concern nowadays with the grid codes requiring efficient control of both positive-sequence and negative-sequence reactive current in a droop fashion as described in [16].

In an MMC-based STATCOM, the energy balancing within the converter is of utmost importance for its proper operation. Apart from the control of the total energy stored in the MMC [17], many studies have focused on the development of the decoupled leg and arm energy controllers to ensure

internal balance both in the case of unavoidable internal parameter mismatches and most importantly for grid disturbances. More specifically, in [18], each arm capacitor voltage is controlled independently by applying a decoupling transformation of the quadratic voltages to define four power components, each one controlled by one current component. In other studies, it has been extensively shown that the DC component of the circulating current can be used to distribute power among the phase legs of the converter, thus achieving leg energy balancing, while the fundamental frequency component of the circulating current is responsible for exchanging power between the upper and lower arm of each phase leg [19–24].

Based on this finding, a method was proposed in which one controller regulates the sum of the upper and lower arm stored energies, while a second controller regulates the difference between them [19]. This control approach can be carried out either using phase coordinates in a nonrotating reference frame [19] or by using a Decoupled Double Synchronous Reference Frame (DDSRF) current control technique to independently control the differential current active and reactive components separated into harmonics and sequences [25]. Moreover, to improve the dynamics of the energy balancing, feed-forward terms of the predicted components can be used [26].

Although the energy balancing between legs is straightforward, the arm balancing is a more complicated task. As first noted in [27], the injection of current in one arm will inevitably affect the energy levels of the arms of the other two phases if no action is taken. The main idea of the decoupled arm energy balancing controller is the injection of active current in the unbalanced phase and reactive currents in the balanced phases so that the total average energy difference remains unaffected. However, the complexity of the solution in [27] is relatively high. More specifically, state-feedback control was employed for arm balancing. Apart from that, Linear-Quadratic Regulator (LQR) design was used to optimize the tuning of the state-feedback controller using the discretized state-space representation of the system in [27]. The method is known to provide very good response. However, it is usually employed along with a state observer, which increases the implementation effort and requires a precise model of the system, in order to operate as designed.

The same control idea has been extensively used in the literature for different MMC applications. In [28], the same approach is used for energy storage systems, where the MMC submodule capacitors are replaced by batteries. Compared to the capacitors, the batteries give higher flexibility in operation due to the higher available power in the converter. Moreover, this study does not consider AC grid unbalances, and the proof-of-concept is given only using simulations. In [29], where batteries are also used, the average State Of Charge (SOC) of the battery modules is used as a reference for the PI controller to change the power distribution of the three phases, and leg energy balancing is achieved through Zero-sequence Voltage Injection (ZVI). A hybrid power approach is used similar to the one proposed in [27], along with DC component Voltage Redistribution (DVR), fundamental current injection and ZVI, which complicate the control structure and its implementation and tuning procedure.

In the present study, a more intuitive method is used to decouple the arm energy controller, based on the idea introduced in [27], using PI controllers that are more easily implemented. The hereby used approach is very similar to the one implemented in [23,30,31], as well as to [32], in which negative sequence circulating current injection is used for the arm energy balancing. However, compared to the present study, these studies lack experimental verification. Moreover, many studies consider balanced AC grid conditions, neglecting the negative impact of AC faults on the MMC balancing, which is crucial especially in STATCOM applications [32,33]. Furthermore, [31] presents a control method for leg energy balancing, which requires manipulation of the negative sequence of the grid current, and thus, this method cannot comply with the LVRT requirements as defined by recent grid codes [34].

The main contribution of the paper is the investigation, implementation and verification of a simple control method, solely based on PI controllers, for internal balancing of an MMC-STATCOM under unbalanced grid conditions, while at the same time Low-Voltage Ride-Through (LVRT) is provided according to the most recent grid codes [34]. Unlike previous studies, this study focuses on the proof-of-concept of the control method using extensive experimental results of the MMC operation

for different cases of AC contingencies, which are considered crucial in such studies, since simulation studies are based on average models, neglecting the non-linear effects of the modulation and the relative delays of the closed loop systems. For this purpose, a DS-MMC STATCOM laboratory set-up was developed. The laboratory configuration under investigation is presented in Figure 1. An AC controllable source, emulating the AC grid, was used to create the voltage sags. Only asymmetrical voltage sags at different voltage levels on Phase-a and Phase-b were investigated. Although the faults are indicated in Figure 1 as solid connections through switches to the ground, in the performed tests, the voltage sags were created by controlling the AC voltage output of the source.

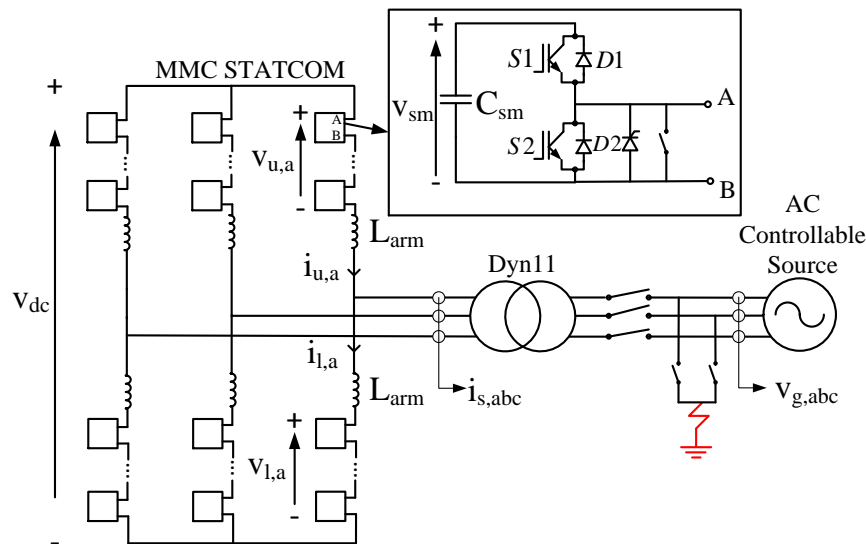


**Figure 1.** Modular Multilevel Converter (MMC)-based Static Synchronous Compensator (STATCOM) connection.

In Section 2, the control system is theoretically presented with the focus laid on the internal controllers. In Section 3, the internal control scheme is experimentally validated. In Section 4, the internal energy balancing of the converter during LVRT is experimentally assessed under different case scenarios. The importance of the internal control scheme is highlighted compared to the uncontrolled case. Finally, Section 5 summarizes the main outcomes of the presented work.

## 2. Internal Control System

An overview of the control system of the MMC can be seen in Figure 2. The outer controllers of an MMC do not differ from those of a conventional two-level converter, and thus, they are not further described. This section focuses on the internal control of the MMC, which is unique in the MMC topology.

The experimental setup parameters, which were also used for the simulations in this section, are shown in Table 1. It should be pointed out that the definition of the plant function is crucial for the control design procedure. Given the plant function and taking into account the system parameters and the associated delays, the tuning of the PI controllers can be performed for each system following the fundamental rules of cascaded linear controllers.

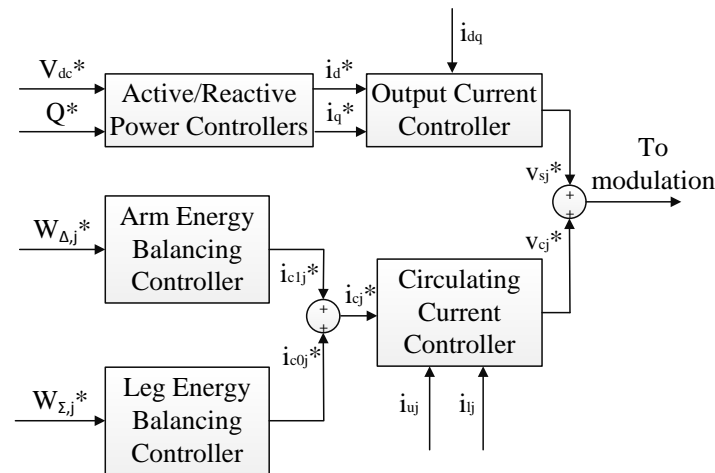


Figure 2. Overview of the MMC STATCOM control system.

Table 1. Parameters of the MMC STATCOM setup.

Description	Symbol	Value
Rated Power (kVA)	$S$	1.25
Rated RMS Voltage (V)	$V_{AC}$	150
Rated DC Voltage (V)	$V_{DC}$	300
Submodule's Capacitance (mF)	$C_{sm}$	4
Arm Inductance (mH)	$L_{arm}$	20
Number of Submodules per arm	$N$	4
Transformer Turns Ratio	$n$	$1:\sqrt{3}$

### 2.1. Leg Energy Balancing Controller

The leg energy balancing controller controls the total stored energy in the converter's legs. If this is shared equally among the legs, all of the capacitors are charged up to the same voltage level. Using the mathematical equations that describe the upper and lower arm power and neglecting the resulting oscillating terms, the average total energy in one leg is given by (1):

$$\frac{\partial W_{\Sigma,j}}{\partial t} = i_{c0j} v_{DC} - \hat{v}_{sj} \hat{i}_{sj} \cos(\phi_{i,j}) \quad (1)$$

Equation (1) reveals that the DC component of the circulating current is responsible for exchanging active power between the converter legs, since the second term of (1) is zero in an STATCOM application. Based on this finding, a PI controller is introduced to provide the reference for the desired energy sum [35]. The reference is usually set by (2):

$$W_{\Sigma,j}^* = 2N \frac{1}{2} C_{sm} V_{sm}^2 \quad (2)$$

The closed loop system used for tuning the leg energy controller is shown in Figure 3. The Laplace transformation of (1) gives directly the plant function of the loop. The PI controller is then tuned to achieve a closed loop bandwidth that gives the desired 30-ms rise time, relatively slow in comparison with the inner circulating current shown in Figure 2. Despite the existence of an integrator in the calculation of  $W_{\Sigma}$  from (1), the leg energy controller uses an integral part to eliminate expected static errors in the average energy level [19].

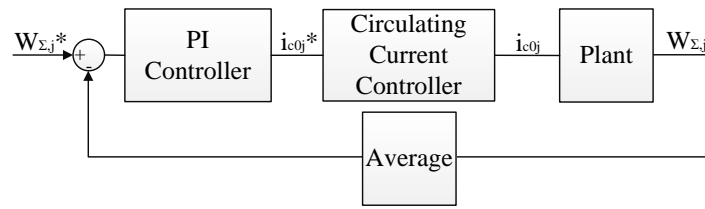


Figure 3. Leg energy balancing closed loop control system.

## 2.2. Decoupled Arm Energy Balancing Controller

The arm energy balancing controller ensures a balanced operation between the upper and lower arm of each leg by controlling the total energy stored in each of them. If the circulating current is assumed to be the superposition of a DC component and a fundamental frequency component, the energy difference between the arms can be expressed as:

$$\frac{\partial W_{\Delta j}}{\partial t} = -\hat{v}_{sj} \hat{i}_{c1j} \cos(\phi_{c,j}) \quad (3)$$

Based on (3) and as noted in [22], the fundamental component of the circulating current is responsible for exchanging active power between the converter's arms. The arm energy controller can be implemented using a PI controller with a similar bandwidth as the leg energy controller [21].

In this paper, a comprehensive and intuitive method is implemented to decouple the arm energy controller based on the idea introduced in [27]. Hereby, only an unbalance in Phase-a is considered in Figure 4, but the result is valid for the other phases, as well, due to the high degree of symmetry.

Due to the double-star topology of the MMC STATCOM with the absence of a physical DC-link, the sum of the vectors of the circulating currents of all phases naturally sums up to zero:

$$\mathbf{i}_{c1a} + \mathbf{i}_{c1b} + \mathbf{i}_{c1c} = \mathbf{0} \quad (4)$$

As a result, an injection of fundamental circulating current in one arm of the MMC phase leg would unavoidably couple with the other phases of the converter, if no further action is taken. To achieve a decoupled control, the main idea of this implementation is the injection of active current in the unbalanced phase and reactive currents in the balanced phases so that the average of the capacitor voltages is not shifted, and thus, the total average energy difference remains unaffected. In this example, since Phase-a is unbalanced, an active current (in phase with the voltage of Phase-a) should be applied as shown in Figure 4. The reactive currents of Phase-b and Phase-c could be combined to form a vector that is opposite the active vector of Phase-a, as shown in Figure 4. The magnitude of the vectors to be applied can be determined based on the law of cosines and basic trigonometry. Therefore, the amplitude of the vectors of Phase-b and Phase-c are  $\sqrt{3}$ -times smaller than the vector of Phase-a. In Figure 4, axis-qb- is denoted as the reactive axis of Phase-b in the anti-clockwise direction. Similarly, axis-qc+ is the reactive axis of Phase-c in the clockwise direction.

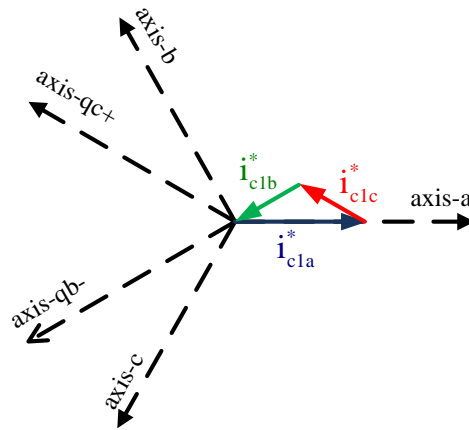


**Figure 4.** Arm energy balancing controller current vectors for decoupled operation.

If a PI controller is used with a gain  $K_{p,arm}$  and a small integral gain  $K_{i,arm}$ , the final commanded current reference for all phases is given by the following Equation (3). If there is an unbalance between the energies of the upper and lower arm of a phase leg  $j$  then  $e_j \neq 0$ , while if balanced,  $e_j = 0$ . In this example,  $e_a \neq 0$ , while  $e_b, e_c = 0$ . It should be clear from (3) that a possible unbalance in, e.g., Phase-a produces an error  $e_a$  and the need for a fundamental component of the circulating current in Phase-a (first term of the first equation). At the same time, a fundamental component in Phase-b and Phase-c is also commanded by the error  $e_a$ , aligned with the respective phase-reactive axes in positive sequence as shown in Figure 4 (second term of the second and third expression) to create a vectorial triangle that will cancel out the unbalance.

$$\begin{aligned} i_{c1a}^* &= (K_{p,arm} + K_{i,arm} \int dt) (e_a \cos(\omega_1 t) + \frac{1}{\sqrt{3}} e_b \cos(\omega_1 t + \frac{\pi}{2}) + \frac{1}{\sqrt{3}} e_c \cos(\omega_1 t - \frac{\pi}{2})) \\ i_{c1b}^* &= (K_{p,arm} + K_{i,arm} \int dt) (e_b \cos(\omega_1 t - \frac{2\pi}{3}) + \frac{1}{\sqrt{3}} e_a \cos(\omega_1 t - \frac{7\pi}{6}) + \frac{1}{\sqrt{3}} e_c \cos(\omega_1 t - \frac{\pi}{6})) \\ i_{c1c}^* &= (K_{p,arm} + K_{i,arm} \int dt) (e_c \cos(\omega_1 t + \frac{2\pi}{3}) + \frac{1}{\sqrt{3}} e_a \cos(\omega_1 t + \frac{7\pi}{6}) + \frac{1}{\sqrt{3}} e_b \cos(\omega_1 t + \frac{\pi}{6})) \end{aligned} \quad (5)$$

Note: The reactive axes of Phase-a are at  $+\frac{\pi}{2}$  and  $-\frac{\pi}{2}$ ; the reactive axes of Phase-b are at  $-\frac{7\pi}{6}$  and  $-\frac{\pi}{6}$ ; the reactive axes of Phase-c are at  $+\frac{7\pi}{6}$  and  $+\frac{\pi}{6}$ .

For simplification reasons and for lower computational effort in the calculation of the references of the circulating current fundamental component, the authors assume that the positive sequence voltage is significantly larger in magnitude than the negative sequence voltage, which is the case in most AC faults, as the experiments shown in Section 4. In the rare case when the positive and the negative sequences have similar magnitudes [36], the simplification would result in an imperfect decoupling of the arm currents. However, this error would be dealt with by the action of the integral part of the arm energy balancing controller.

The closed loop system for tuning the arm energy balancing controller is shown in Figure 5. The plant function for this controller is derived by the Laplace transformation of (3), and the bandwidth is set appropriately in order to achieve a rise time of approximately 30 ms.

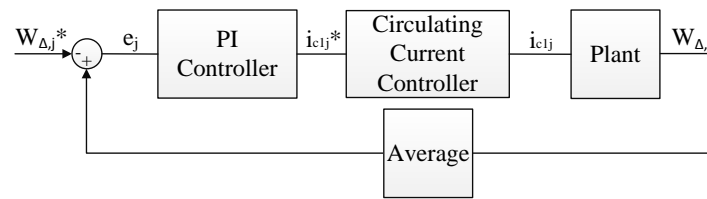


Figure 5. Arm energy balancing closed loop control system.

### 2.3. Circulating Current Controller

In an STATCOM application, the average circulating current is zero since there is no exchange of active power between the DC and the AC side. However, as noted in [22], the circulating current of an MMC presents naturally a second order harmonic component when the current of fundamental frequency is controlled. Apart from that, as noted previously, to ensure balanced operation between the legs of the MMC, the circulating current controller should be able to follow a DC, as well as a fundamental component reference.

In total, the circulating current controller needs to present high gain at 0 Hz, 50 Hz and 100 Hz. In order to achieve this, the control scheme shown in Figure 6 is employed, utilizing resonant controllers connected in parallel and tuned at the respective frequencies. The analytical control design procedure for the circulating current controller is shown in [37].

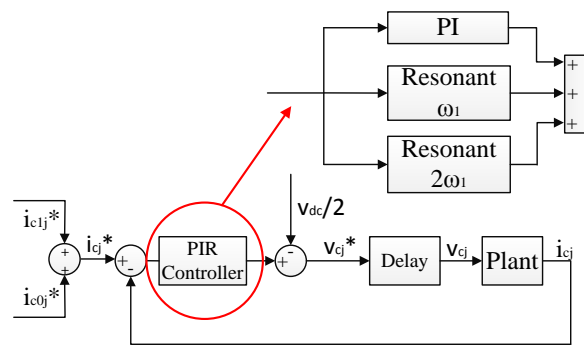


Figure 6. Circulating current controller.

The delay block is used to model the associated input delays, such as the Pulse Width Modulation (PWM) delay and the computational delay of the digital controller. The plant function of the circulating current controller is given by (6):

$$\frac{i_c}{v_c} = \frac{1}{L_{arm}s + R_{arm}} \quad (6)$$

The proportional gain is tuned based on the desirable bandwidth of the control system, which is imposed by the desirable rise time and is limited by the inherited delays of the control system, as shown in (7).

$$\frac{\ln(9)}{t_{r_{max}}} < \omega_{bw} < \frac{\omega_s}{10} \quad (7)$$

### 3. Experimental Validation of Internal Control

Simulation results of MMC-STATCOM under different cases of grid unbalances at higher voltages have been previously presented in [37]. However, experimental verification is considered crucial to prove the validity of the proposed control scheme, considering the delays and non-linearities of the real system. This section presents experimental results that verify the validity of the previously-described control system. The current experimental work is performed in a small-scale laboratory setup, shown in Figure 7 with the specifications noted in Table 1. The converter is connected to an AC source through



a Dyn 11 isolation transformer (DANTRAFO A/S, Horsens, Denmark), and the dSPACE platform (dSPACE GmbH, Paderborn, Germany) is used to implement the control scheme and record the results. The control parameters used for the experiments are presented in Table 2.



**Figure 7.** Laboratory prototype of the MMC STATCOM.

**Table 2.** Control parameters of the experimental setup.

Controller	$K_p$	$K_i$	$K_r$
Arm Energy Controller ( $W_\Delta$ )	0.2	0.5	-
Leg Energy Controller ( $W_\Sigma$ )	0.2	0.3	-
Circulating Current Controller	32.2	$3.22 \times 10^3$	$\omega_1: 3.22 \times 10^3$ $\omega_2: 3.22 \times 10^3$
Output Current Controller	24.2	$2.42 \times 10^3$	-

At first, the effect of the leg energy balancing controller is demonstrated in Figure 8. The parameters of the setup are similar for all phases, and therefore, only a small difference exists between the leg's sum energies. When the controller is activated, this difference is eliminated.

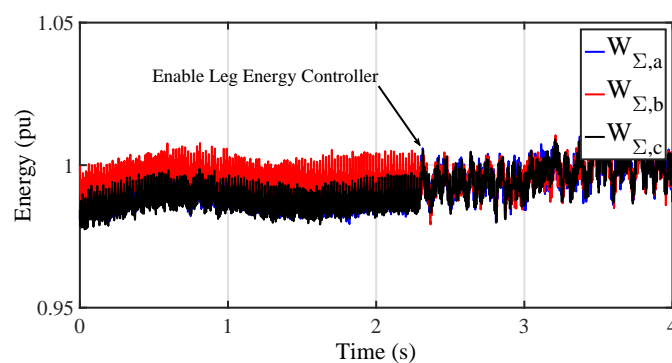


**Figure 8.** Leg energy controller experimental effect.

The controller's performance is shown in simulation and experimentally in Figure 9a,b, respectively, by applying an energy step of +10% in Phase-a, while Phase-b and Phase-c receive a −5% command. In this way, the leg energy controller causes the energy to flow out of Leg-b and Leg-c and into Leg-a. The controller is tuned for a rise time of approximately 30 ms.

The arm energy balancing controller effect is evaluated in Figure 10. Initially, the energy oscillates between the arms of each leg. After the controller activation, the arm energy difference remains at zero, and the stability of the converter is enhanced. In Figure 11a, the step response of the arm energy

balancing controller is simulated, while in Figure 11b, it is demonstrated experimentally. The controller is tuned for a rise time of 30 ms, and a step change of 10% in the energy difference of the arms of Phase-a is applied. The controller reacts as expected, and its decoupled performance is verified, as Phase-b and Phase-c are not affected by the change in the energy difference of Phase-a.

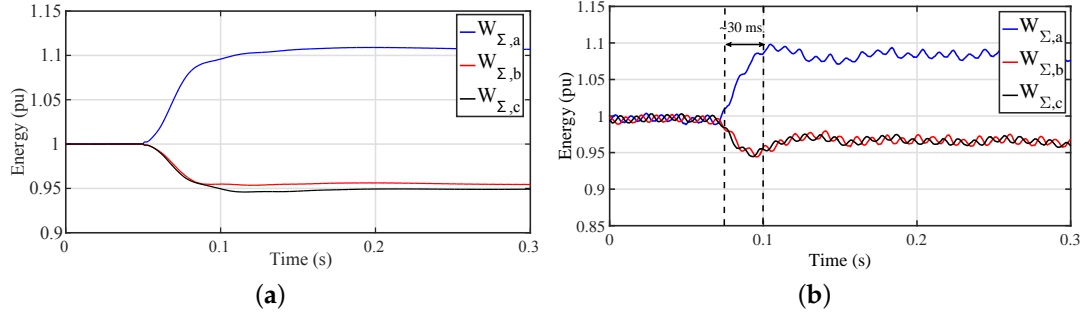


**Figure 9.** Leg energy controller step response (a) in simulation and (b) experimental performance.

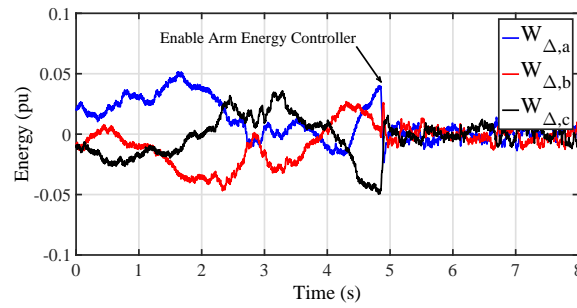


**Figure 10.** Arm energy controller experimental effect.

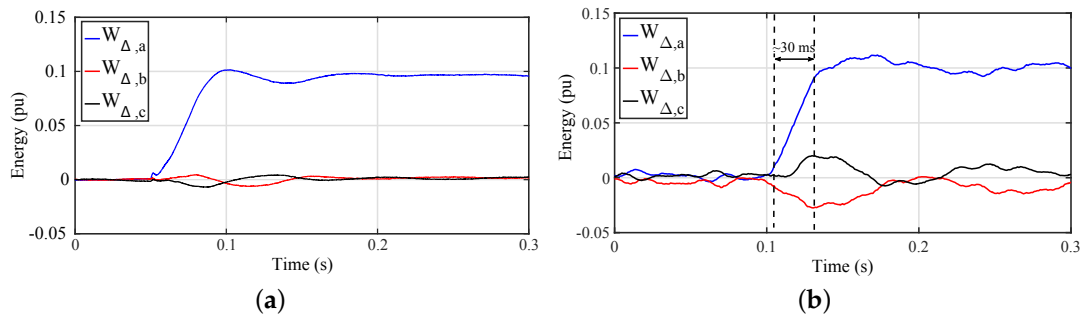


**Figure 11.** Arm energy controller step response (a) in simulation and (b) experimental performance.

#### 4. Low-Voltage Ride-Through of the MMC STATCOM

Generally, under unbalanced conditions, the established instantaneous power theory [38] is applicable:

$$\begin{cases} p = P_0 + \hat{P}_1 \cos(2\omega_1 t) + \hat{P}_2 \sin(2\omega_1 t) \\ q = Q_0 + \hat{Q}_1 \cos(2\omega_1 t) + \hat{Q}_2 \sin(2\omega_1 t) \end{cases} \quad (8)$$

As can be observed, (8) contains the average terms  $P_0$  and  $Q_0$ , as well as the oscillating terms  $\hat{P}_1$ ,  $\hat{P}_2$ ,  $\hat{Q}_1$  and  $\hat{Q}_2$ . The oscillating terms are the result of the presence of the negative sequence voltage component.

Applying the dq-transformations and taking into consideration both the positive and the negative sequence components, the power terms can be written in matrix form, as shown in (9). From (9), it can be seen that there are six power terms that can be controlled and only four independent variables.

Moreover, (9) shows that any change in the positive or negative sequence current component results in active and reactive power oscillations, as long as negative sequence voltage is present, e.g., in asymmetrical AC faults.

$$\begin{bmatrix} P_0 \\ \hat{P}_1 \\ \hat{P}_2 \\ Q_0 \\ \hat{Q}_1 \\ \hat{Q}_2 \end{bmatrix} = \frac{3}{2} \begin{bmatrix} V_d^+ & V_q^+ & V_d^- & V_q^- \\ V_d^- & V_q^- & V_d^+ & V_q^+ \\ V_q^- & -V_d^- & -V_q^+ & V_d^+ \\ V_q^+ & -V_d^+ & V_q^- & -V_d^- \\ V_q^- & -V_d^- & V_q^+ & -V_d^+ \\ -V_d^- & -V_q^- & V_d^+ & V_q^+ \end{bmatrix} \cdot \begin{bmatrix} i_d^+ \\ i_q^+ \\ i_d^- \\ i_q^- \end{bmatrix} \quad (9)$$

In case of faults on the AC-side, injection of positive sequence capacitive current is required to support the recovery of the Point of Common Coupling (PCC) voltage, while the injection of negative sequence inductive current supports the grid by reducing the negative sequence voltage at the PCC.

Recent grid codes suggest that when an AC fault arises, the converter should be able to avoid tripping while injecting capacitive positive sequence reactive current according to (10). This is usually referred to as Positive Sequence Injection Low-Voltage Ride-Through (PSI-LVRT):

$$i_q^+ = k^+ (0.9 - V^+) \quad (10)$$

where  $V^+$  is given in pu at the PCC and  $k^+$  usually takes values within the interval (0–10). It can be deduced that a 10% dead-band is considered in (10) [39].

As highlighted in [40], the injection of positive sequence current does not reduce the unbalance at the PCC, so recent grid codes require the injection of inductive negative sequence current proportional to the negative sequence voltage at the PCC, according to (11) [16]:

$$i_q^- = -k^- (V^- - 0.05) \quad (11)$$

where  $V^-$  is given in pu at the PCC and  $k^-$  usually takes values within the interval (0–10). A dead-band of 5% is considered in this case. When both positive and negative sequence currents are injected, the injection strategy is commonly referred to as Mixed Sequence Injection Low-Voltage Ride-Through (MSI-LVRT).

In this section, experimental results evaluate the control structure of MMC under grid disturbances in the three test case scenarios listed below:

1. Experimental Scenario 1: 95% voltage sag in Phase-a with PSI-LVRT.
2. Experimental Scenario 2: 95% voltage sag in Phase-a with MSI-LVRT.
3. Experimental Scenario 3: 95% voltage sag in Phase-a and 50% voltage sag in Phase-b with PSI-LVRT.

The tested voltage sags were applied by defining the voltage level, the start time and the duration of the sag at the respective phase through the controllable AC source, as shown in Figure 1. In every case, experimental results evaluate the performance of the MMC STATCOM with and without the insertion of the described energy controllers. It should be noted that the control system is implemented using the dSPACE environment. The sampling frequency used in the control model of MATLAB/Simulink (2015a, MathWorks, Natick, MA 01760-2098, USA), which is compiled in dSPACE is 20 kHz. Due to the large number of result points obtained, downsampling was necessary for the depiction of the results in the ControlDesk of dSPACE. As a result, the data are presented in the figures of this manuscript with a sampling rate of 1 kHz. Regarding the effective frequency of a submodule, this was defined by the sorting algorithm used for the capacitor voltage balancing. This value was monitored at all times of the control operation, and it varied between 800 Hz and 1 kHz.

#### 4.1. Experimental Scenario 1

In the first case scenario, an asymmetrical voltage sag occurs at the AC-side of the MMC STATCOM for 300 ms. Phase-a voltage is reduced to 5% of its value, while Phase-b and Phase-c remain unaffected, as shown in Figure 12.

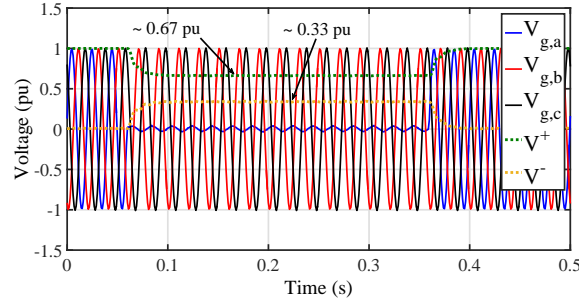


**Figure 12.** AC voltage waveforms for Experimental Scenario 1.

In this first scenario, only positive sequence current injection is considered, and according to (10) and the measured  $V^+$ , for  $k^+ = 2.5$ , approximately 0.6 pu capacitive reactive current is injected as shown in Figure 13a. It should be noted that based on these waveforms, the current does not surpass its rated values. The peak value of the currents observed at the end of the transient are caused due to the inevitable delays in the decomposition of the voltage sequences by the phase locked loop. It is also worth noting that the injected currents of all three phases, during the transient, are symmetrical due to the PSI followed in this experimental scenario. The distortion of the currents is at the sixth harmonic and its multiples and could be associated, on the one hand, with the effect of dead-time and inverter non-linearities and, on the other hand, with a slight difference between the energies of the arms of the converter system, as shown in Figure 14b. The distortion in the current before the injection could be also attributed to the same reasons.

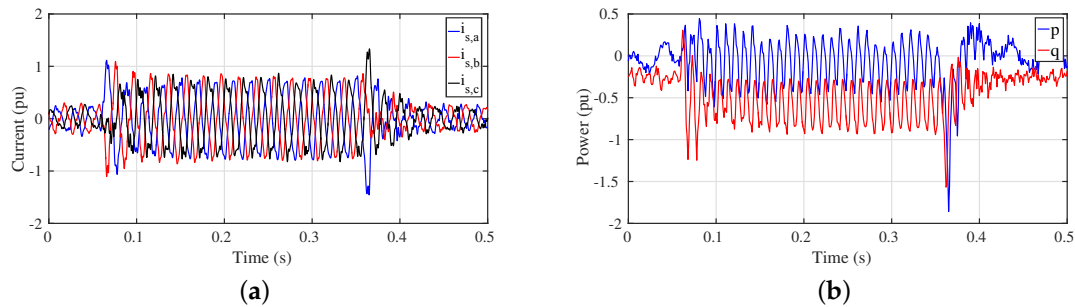


**Figure 13.** (a) Current waveforms and (b) instantaneous p and q waveforms for Scenario 1.

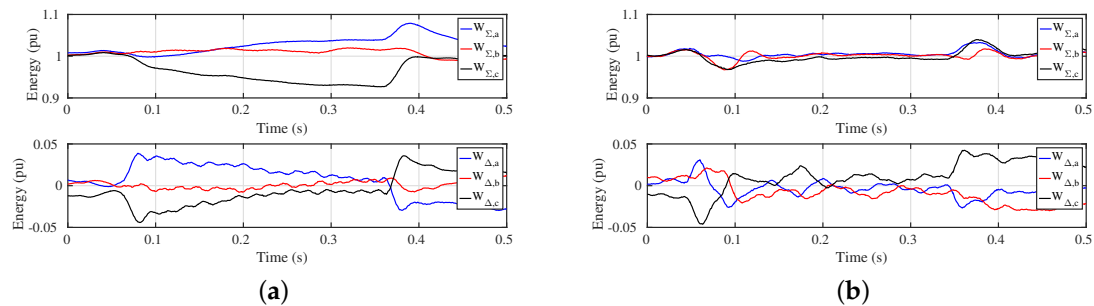


**Figure 14.** (a)  $W_{\Sigma}$  and  $W_{\Delta}$  for Scenario 1 without energy controllers and (b) with energy controllers.

As is depicted in (8) and (9), the presence of negative sequence voltage results in active and reactive power oscillations. These oscillations during the voltage sag can be seen in Figure 13b, where the instantaneous active and reactive powers are plotted. During the sag, the average reactive power is negative, which in this case indicates capacitive operation of the converter. Furthermore, the active and reactive power exhibit peak values when the converter returns to normal operation, mainly due to the aforementioned Phase-Locked Loop (PLL) delay in the decomposition of the voltage sequences. These peaks, however, occur for a short period of time ( $\sim 10$  ms) and therefore do not cause a problem in the operation of the MMC.

The internal balance of the MMC is assessed by the sum of the upper and lower arm total energies ( $W_{\Sigma}$ ), as well as their difference ( $W_{\Delta}$ ), as these reflect directly on the capacitors' voltages. Firstly, in Figure 14a,  $W_{\Sigma}$  and  $W_{\Delta}$  are shown for every phase, when the energy balancing controllers are not activated.

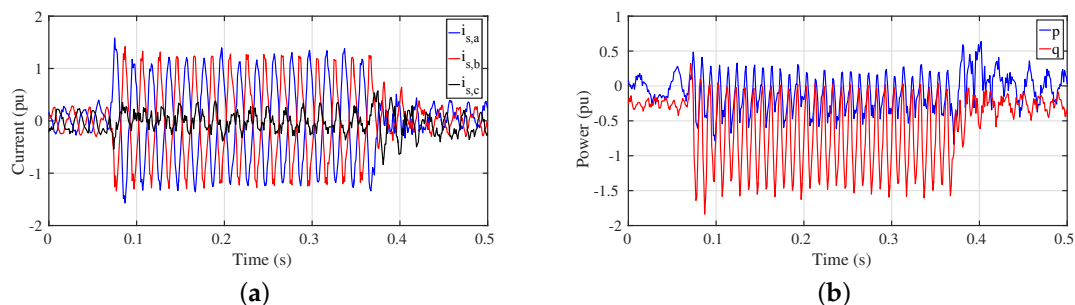
An unbalance between the converter legs can be observed in Figure 14a. More particularly, Phase-c delivers energy to Phase-a and Phase-b. In this way, the capacitors of Phase-c get discharged while the ones of Phase-a and Phase-b get charged, which may result in converter tripping, if the fault persists. The difference of the energies between the upper and lower arm present in this case acceptable performance.

Figure 14b depicts  $W_{\Sigma}$  and  $W_{\Delta}$  when the energy controllers are activated. The leg energy balancing controller manages to eliminate the energy differences between the converter legs and keep them equal at 1 pu. The arm energy controller exhibits an improved performance in comparison to the previous case, as it acts quickly after the initial transient, keeping the energy levels of the upper and lower arms of each phase equal.

#### 4.2. Experimental Scenario 2

In the second case scenario, the fault is identical to the one applied in the previous case, with the Phase-a voltage reducing to 5% of its initial value. The resulting AC-voltage waveforms are therefore as depicted in Figure 12. In this case however, the MMC STATCOM will be tested for MSI-LVRT.

The positive sequence current droop controller is set again to  $k^+ = 2.5$ , while the one for the negative sequence current is chosen to be  $k^- = 1$ . As a result, the required capacitive positive sequence current is again found to be approximately 0.6 pu, while the inductive negative sequence current required, according to (11), is 0.28 pu. The injected current waveforms are shown in Figure 15a. Note that in this case, the currents are increased due to the negative sequence injection, but remain inside their rated limits. It is also evident that during the sag, the MSI strategy results in unbalanced current injection. Figure 15b shows the instantaneous active and reactive powers. Due to the increased current injection, the power oscillations increased. This result can also be explained by (9).



**Figure 15.** (a) Current waveforms and (b) instantaneous p and q waveforms for Scenario 2.

Moreover, similarly to the previous scenario, the internal balance of the converter and its ability to ride through the AC-fault without tripping is assessed at this point. Firstly, the waveforms of  $W_{\Sigma}$  and  $W_{\Delta}$  when the energy controllers are deactivated are shown in Figure 16a. In this figure, it can

be seen that the leg energy of Phase-b increases unacceptably, and by the end of the voltage sag, it reaches 1.15 pu. Furthermore, an inspection of the energy difference between the arms shows that an unbalance exists between the upper and lower arm.

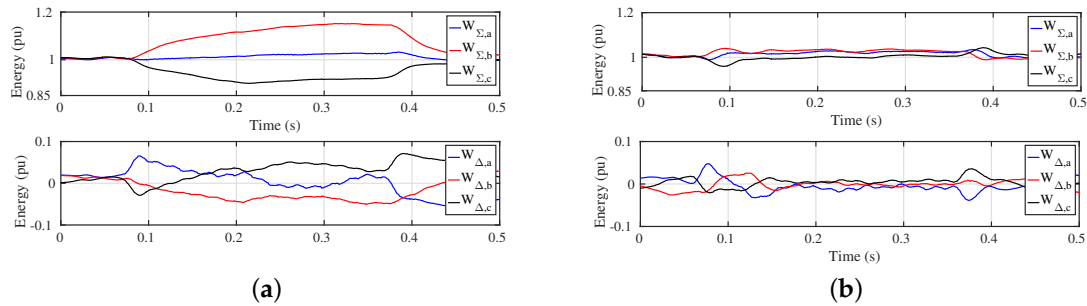


**Figure 16.** (a)  $W_{\Sigma}$  and  $W_{\Delta}$  for Scenario 2 without energy controllers and (b) with energy controllers.

On the other hand, Figure 16b depicts the waveforms of  $W_{\Sigma}$  and  $W_{\Delta}$  when the energy controllers are activated. A simple inspection of the waveforms reveals that the energy controllers manage to keep all three MMC legs, as well as their arms balanced after an initial transient. This operation apparently ensures the safe LVRT of the converter under AC faults.

#### 4.3. Experimental Scenario 3

In the final tested scenario, a more severe asymmetrical voltage sag occurs at the AC-side of the MMC STATCOM for 300 ms. Phase-a voltage is reduced again to 5% of its value, and Phase-b experiences a voltage sag of 50%, while Phase-c remains unaffected, as shown in Figure 17.

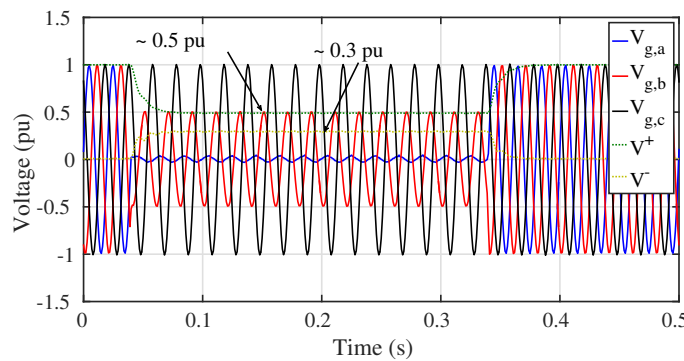


**Figure 17.** AC voltage waveforms for Experimental Scenario 3.

The applied voltage sag causes the positive sequence voltage vector to reduce to 0.5 pu as shown in Figure 17. This scenario considers again a PSI-LVRT and according to (10), the required capacitive positive sequence current for  $k^+ = 2.5$  is 1 pu. The resulting current waveforms are shown in Figure 18a.

Once again, due to the emergence of the negative sequence voltage vector, the instantaneous active and reactive powers will present severe oscillations that due to the high current injection are larger in comparison to the first tested scenario (see Figure 13b). Figure 18b depicts the aforementioned power waveforms. It can be noted that the average injected reactive power is 1 pu. In this figure, the active and reactive power waveforms exhibit again severe peaks that exceed 2 pu. As explained before, these peaks are the result of a delayed sequence separation and should not cause a problem in the operation of the converter system, as they appear for a very short duration.

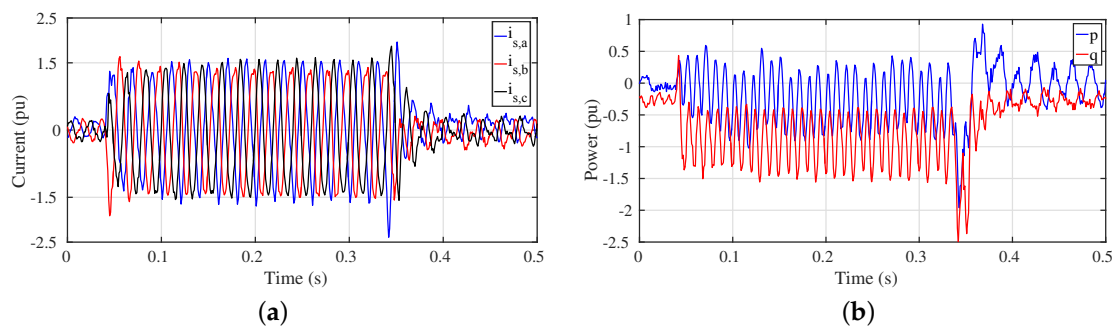


**Figure 18.** (a) Current waveforms and (b) instantaneous p and q waveforms for Scenario 3.

In Figure 19a, the energy controllers are deactivated. During the voltage sag, severe unbalance between the energy levels of the converter legs is noticed. At the same time, the arm voltages seem to drift away in this case. In particular, Phase-b upper arm energy is increased in comparison to the lower arm, resulting in an unacceptable operation of the MMC STATCOM.

In Figure 19b, the energy controllers are activated, and the improvement on the resulting energy waveforms is evident. The leg energy balancing controller acts quickly, bringing the total leg energies together and keeps each phase energy level at approximately 1 pu. The arm energy balancing controller brings the energy difference levels close to zero as expected, after an initial transient that causes unbalance between the arms, ensuring the safe LVRT of the MMC STATCOM.

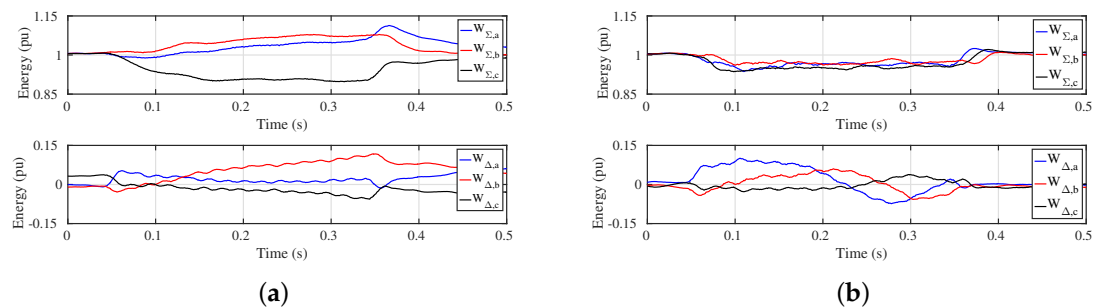


**Figure 19.** (a)  $W_{\Sigma}$  and  $W_{\Delta}$  for Scenario 3 without energy controllers and (b) with energy controllers.

## 5. Conclusions

This paper focused on the identified problem of internal balancing of a DS-MMC STATCOM under unbalanced grid conditions, while investigating the LVRT response of the converter. The most recent grid codes were used as the reference to determine the positive and negative output current injection values for different types of voltage sags. The chosen voltage sag scenarios were carried out experimentally, and the proposed leg and arm energy balancing controllers' performance was tested using a developed laboratory setup, taking into account all of the non-linearities of the modulation and the delays of the real system.

At first, the step response of the leg and arm energy balancing controllers was tested in normal operation. The structure of the developed controllers simplified their implementation in the experimental setup and allowed the fast proper tuning of the closed-loop system. During the different tests of voltage sags, the arm and leg energies were monitored with and without the use of the energy controllers. The results showed the problem of energy balancing in case no energy controllers were used and highlighted the improved performance of the MMC STATCOM when the energy controllers are activated. In all of the tested cases, the converter managed to ride through the fault successfully, while at the same time keeping its internal balance.



**Author Contributions:** Georgios Tsolaridis and Epameinondas Kontos designed, performed the experiments and were responsible for writing the paper. Sanjay K. Chaudhary and Remus Teodorescu were supervising the experiments and provided insight in the data analysis. Pavol Bauer contributed in the paper editing and ascertained the quality of the data analysis.

**Conflicts of Interest:** The authors declare no conflict of interest.

## Nomenclature

$\cos(\phi_{c,j})$	Phase angle of the circulating current vector in phase $j$
$\cos(\phi_{i,j})$	Phase angle of the output current vector in phase $j$
$C_{sm}$	Submodule capacitance
$e_j$	Phase errors of $W_{\Delta,j}$ fed to the arm energy controller
$i_{cj}$	Circulating current in phase $j$
$i_{c0j}$	DC component of the circulating current in phase $j$
$i_{c1j}^*$	Reference of the first fundamental injected circulating current in phase $j$
$i_{c1j}$	Peak value of the first fundamental injected circulating current in phase $j$
$i_d^+$	d component of the positive sequence output current
$i_d^-$	d component of the negative sequence output current
$i_{lj}$	Lower arm current of phase $j$
$i_q^+$	q component of the positive sequence output current
$i_q^-$	q component of the negative sequence output current
$i_{sj}$	Output current in phase $j$
$i_{uj}$	Upper arm current of phase $j$
$k^+$	Slope of the droop controller for $i_q^+$ injection
$k^-$	Slope of the droop controller for $i_q^-$ injection
$K_{i,arm}$	Integral gain of arm energy controller
$K_{p,arm}$	Proportional gain of arm energy controller
$L_{arm}$	Arm inductance
$N$	Number of submodules per converter arm
$n$	Transformer turns ratio
$P_{0,1,2}$	Average active power term and the oscillating terms on the first and second fundamental frequency
$Q_{0,1,2}$	Average reactive power term and the oscillating terms on the first and second fundamental frequency
$S$	Rated power of the converter
$t_{r,max}$	Maximum rise time according to the design requirements
$V_{AC}$	Rated RMS voltage of the converter
$v_{cj}$	Circulating voltage in phase $j$
$V_d^+$	d component of the positive sequence voltage vector at the PCC
$V_d^-$	d component of the negative sequence voltage vector at the PCC
$v_{DC}$	Pole-to-pole DC voltage
$v_{gj}$	AC grid phase voltage at the grid/source
$v_{lj}$	Lower arm voltage of phase $j$
$V_q^+$	q component of the positive sequence voltage vector at the PCC
$V_q^-$	q component of the negative sequence voltage vector at the PCC
$v_{sj}$	Output voltage in phase $j$
$v_{sm}$	Submodule capacitor voltage
$v_{uj}$	Upper arm voltage of phase $j$
$W_{\Delta,j}$	Energy difference between the arms in phase leg $j$
$W_{\Sigma,j}$	Total energy in phase leg $j$
$\omega_{bw}$	Bandwidth of the circulating current controller
$\omega_s$	Switching angular frequency
$\omega_1$	Fundamental angular frequency



## References

1. Hagiwara, M.; Maeda, R.; Akagi, H. Negative-sequence reactive-power control by the modular multilevel cascade converter based on double-star chopper-cells (MMCC-DSCC). In Proceedings of the 2010 IEEE Energy Conversion Congress and Exposition (ECCE), Atlanta, GA, USA, 12–16 September 2010.
2. Lesnicar, A.; Marquardt, R. An innovative modular multilevel converter topology suitable for a wide power range. In Proceedings of the 2003 IEEE Bologna Power Tech Conference Proceedings, Bologna, Italy, 23–26 June 2003; Volume 3.
3. Sanz, I.; Moranchel, M.; Bueno, E.J.; Rodriguez, F.J. Analysis of medium voltage modular multilevel converters for facts applications. In Proceedings of the 42nd Annual Conference of the IEEE Industrial Electronics Society (IECON 2016), Florence, Italy, 23–26 October 2016; pp. 6459–6464.
4. Kamran, S.A.; Muñoz, J. Study of a state-of-the art m-statcom. In Proceedings of the 2015 IEEE International Conference on Industrial Technology (ICIT), Seville, Spain, 17–19 March 2015; pp. 2733–2738.
5. Hagiwara, M.; Maeda, R.; Akagi, H. Negative-sequence reactive-power control by a pwm statcom based on a modular multilevel cascade converter (MMCC-SDBC). *IEEE Ind. Appl. Soc.* **2011**, *48*, 720–729.
6. Spahic, E.; Reddy, C.P.S.S.; Pieschel, M.; Alvarez, R. Multilevel statcom with power intensive energy storage for dynamic grid stability - frequency and voltage support. In Proceedings of the 2015 IEEE Electrical Power and Energy Conference (EPEC), London, ON, Canada, 26–28 October 2015; pp. 73–80.
7. Antonopoulos, A.; Svensson, J.R. Evaluation of negative-sequence-current compensators for high-speed electric railways. In Proceedings of the 2016 IEEE Energy Conversion Congress and Exposition (ECCE), Milwaukee, WI, USA, 18–22 September 2016; pp. 1–8.
8. Shang, J.; Dai, N.; Wang, B.; Chen, H. Railway power conditioner based on delta-connected modular multilevel converter. In Proceedings of the 2016 IEEE Energy Conversion Congress and Exposition (ECCE), Milwaukee, WI, USA, 18–22 September 2016; pp. 1–7.
9. Behrouzian, E.; Bongiorno, M.; De La Parra, H.Z. Investigation of negative sequence injection capability in H-bridge multilevel statcom. In Proceedings of the 2014 16th European Conference on Power Electronics and Applications (EPE'14-ECCE Europe), Lappeenranta, Finland, 26–28 August 2014.
10. Akagi, H. Classification, terminology, and application of the modular multilevel cascade converter (MMCC). *IEEE Trans. Power Electron.* **2011**, *26*, 3119–3130.
11. Li, B.; Shi, S.; Xu, D.; Wang, W. Control and analysis of the modular multilevel DC de-icer with statcom functionality. *IEEE Trans. Ind. Electron.* **2016**, *63*, 5465–5476.
12. Vechalapu, K.; Bhattacharya, S. Modular multilevel converter based medium voltage DC amplifier for ship board power system. In Proceedings of the 2015 IEEE 6th International Symposium on Power Electronics for Distributed Generation Systems (PEDG), Aachen, Germany, 22–25 June 2015; pp. 1–8.
13. Pirouz, H.M.; Bina, T.M. A transformerless medium-voltage statcom topology based on extended modular multilevel converters. *IEEE Trans. Power Electron.* **2011**, *26*, 1534–1545.
14. António-Ferreira, A.; Gomis-Bellmunt, O.; Teixidó, M. HvdC-based modular multilevel converter in the statcom operation mode. In Proceedings of the 2016 18th European Conference on Power Electronics and Applications (EPE'16 ECCE Europe), Karlsruhe, Germany, 5–9 September 2016; pp. 1–10.
15. Tsolaridis, G.; Pereira, H.A.; Cupertino, A.F.; Teodorescu, R.; Bongiorno, M. Losses and cost comparison of DS-HB and SD-FB MMC based large utility grade STATCOM. In Proceedings of the 2016 IEEE 16th International Conference on Environment and Electrical Engineering (EEEIC), Florence, Italy, 7–10 June 2016.
16. Wijnhoven, T.; Deconinck, G.; Neumann, T.; Erlich, I. Control aspects of the dynamic negative sequence current injection of type 4 wind turbines. In Proceedings of the 2014 IEEE PES General Meeting Conference & Exposition, National Harbor, MD, USA, 27–31 July 2014.
17. Hu, P.; Jiang, D.; Zhou, Y.; Liang, Y.; Guo, J.; Lin, Z. Energy-balancing control strategy for modular multilevel converters under submodule fault conditions. *IEEE Trans. Power Electron.* **2014**, *29*, 5021–5030.
18. Perez, M.A.; Rodriguez, J.; Bernet, S. Decoupled capacitor voltage control of modular multilevel . In Proceedings of the 2014 IEEE Energy Conversion Congress and Exposition (ECCE), Pittsburgh, PA, USA, 14–18 September 2014.
19. Antonopoulos, A.; Angquist, L.; Nee, H.P. On dynamics and voltage control of the modular multilevel converter. In Proceedings of the 13th European Conference on Power Electronics and Applications, Barcelona, Spain, 8–10 September 2009.

20. Zhang, L.; Tang, Y.; Yang, S.; Gao, F. A modular multilevel converter-based grid-tied battery-supercapacitor hybrid energy storage system with decoupled power control. In Proceedings of the 2016 IEEE 8th International Power Electronics and Motion Control Conference (IPEMC-ECCE Asia), Hefei, China, 22–26 May 2016.
21. Soong, T.; Lehn, P.W. Internal Power Flow of a Modular Multilevel Converter with Distributed Energy Resources. *IEEE J. Emerg. Sel. Top. Power Electron.* **2014**, *2*, 1127–1138.
22. Ilves, K.; Antonopoulos, A.; Norrga, S.; Nee, H.P. Steady-state analysis of interaction between harmonic components of arm and line quantities of modular multilevel converters. *IEEE Trans. Power Electron.* **2012**, *27*, 57–68.
23. Wenig, S.; Rojas, F.; Schönleber, K.; Suriyah, M.; Leibfried, T. Simulation framework for DC grid control and acdc interaction studies based on modular multilevel converters. *IEEE Trans. Power Deliv.* **2016**, *31*, 780–788.
24. Saad, H.; Guillaud, X.; Mahseredjian, J.; Denetiere, S.; Nguefeu, S. Mmc capacitor voltage decoupling and balancing controls. *IEEE Trans. Power Deliv.* **2015**, *30*, 704–712.
25. Bergna, G.; Berne, E.; Egrot, P.; Lefranc, P.; Arzande, A.; Vannier, J.C.; Molinas, M. An energy-based controller for hvdc modular multilevel converter in decoupled double synchronous reference frame for voltage oscillation reduction. *IEEE Trans. Ind. Electron.* **2013**, *60*, 2360–2371.
26. Cui, S.; Lee, H.J.; Jung, J.J.; Lee, Y.; Sul, S.K. A comprehensive AC side single line to ground fault ride through strategy of a modular multilevel converter for hvdc system. In Proceedings of the 2015 IEEE Energy Conversion Congress and Exposition (ECCE), Montreal, QC, Canada, 20–24 September 2015; pp. 5378–5385.
27. Munch, P.; Gorges, D.; Izak, M.; Liu, S. Integrated current control, energy control and energy balancing of modular multilevel converters. In Proceedings of the 36th Annual Conference on IEEE Industrial Electronics Society, Glendale, AZ, USA, 7–10 November 2010.
28. Hillers, A.; Biela, J. Fault-tolerant operation of the modular multilevel converter in an energy storage system based on split batteries. In Proceedings of the 2014 16th European Conference on Power Electronics and Applications, Lappeenranta, Finland, 26–28 August 2014; pp. 1–8.
29. Chen, Q.; Li, R.; Cai, X. Analysis and fault control of hybrid modular multilevel converter with integrated battery energy storage system. *IEEE J. Emerg. Sel. Top. Power Electron.* **2017**, *5*, 64–78.
30. Jung, J.J.; Cui, S.; Kim, S.; Sul, S.K. A cell capacitor energy balancing control of modular multilevel converter considering the unbalanced AC grid conditions. In Proceedings of the 2014 International Power Electronics Conference (IPEC-Hiroshima 2014—ECCE ASIA), Hiroshima, Japan, 18–21 May 2014; pp. 1268–1275.
31. Leon, A.E.; Amodeo, S.J. Energy balancing improvement of modular multilevel converters under unbalanced grid conditions. *IEEE Trans. Power Electron.* **2017**, *32*, 6628–6637.
32. Cui, S.; Kim, S.; Jung, J.J.; Sul, S.K. A comprehensive cell capacitor energy control strategy of a modular multilevel converter (mmc) without a stiff DC bus voltage source. In Proceedings of the 2014 IEEE Applied Power Electronics Conference and Exposition (APEC 2014), Fort Worth, TX, USA, 16–20 March 2014; pp. 602–609.
33. Fan, S.; Zhang, K.; Xiong, J.; Xue, Y. An improved control system for modular multilevel converters with new modulation strategy and voltage balancing control. *IEEE Trans. Power Electron.* **2015**, *30*, 358–371.
34. VDE. VDE-AR-N 4120:2015-01 Technical Requirements for the Connection and Operation of Customer Installations to the High-Voltage Network (TCC High-Voltage); VDE: Frankfurt am Main, Germany, 2015.
35. Vasiladiotis, M.; Cherix, N.; Rufer, A. Impact of grid asymmetries on the operation and capacitive energy storage design of modular multilevel converters. *IEEE Trans. Ind. Electron.* **2015**, *62*, 6697–6707.
36. Prieto-Araujo, E.; Junyent-Ferré, A.; Clariana-Colet, G.; Gomis-Bellmunt, O. Control of modular multilevel converters under singular unbalanced voltage conditions with equal positive and negative sequence components. *IEEE Trans. Power Syst.* **2017**, *32*, 2131–2141.
37. Tsolaridis, G.; Kontos, E.; Parikh, H.; Sanchez, R.; Teodorescu, R.; Chaudhary, S. Control of a modular multilevel converter STATCOM under internal and external unbalances. In Proceedings of the 42nd Annual Conference of the IEEE Industrial Electronics Society (IECON 2016), Florence, Italy, 23–26 October 2016.
38. Akagi, H.; Kanazawa, Y.; Nabae, A. Instantaneous reactive power compensators comprising switching devices without energy storage components. *IEEE Trans. Ind. Appl.* **1984**, *IA-20*, 625–630.

39. Uphues, A.; Nötzold, K.; Griessel, R.; Wegener, R.; Soter, S. Overview of LVRT-capability pre-evaluation with an inverter based test bench. In Proceedings of the 2015 IEEE 24th International Symposium on Industrial Electronics (ISIE), Buzios, Brazil, 3–5 June 2015.
40. Camacho, A.; Castilla, M.; Miret, J.; Guzman, R.; Borrell, A. Reactive power control for distributed generation power plants to comply with voltage limits during grid faults. *IEEE Trans. Power Electron.* **2014**, *29*, 6224–6234.



© 2017 by the authors. Licensee MDPI, Basel, Switzerland. This article is an open access article distributed under the terms and conditions of the Creative Commons Attribution (CC BY) license (<http://creativecommons.org/licenses/by/4.0/>).